

A barotropic model of eddy saturation

NAVID C. CONSTANTINOU*

Scripps Institution of Oceanography, University of California, San Diego, La Jolla, California

ABSTRACT

“Eddy saturation” refers to a regime in which the total volume transport of an oceanic current is insensitive to the wind stress strength. Baroclinicity is currently believed to be key to the development of an eddy-saturated state. Here, we show that eddy saturation can also occur in a purely barotropic flow over topography, without baroclinicity. We show that eddy saturation is a fundamental property of barotropic dynamics above topography. We demonstrate that the main factor controlling the appearance or not of eddy-saturated states is the structure of geostrophic contours, that is the contours of f/H of the ratio of the Coriolis parameter over the ocean’s depth. Eddy-saturated states occur when the geostrophic contours are *open*, that is when the geostrophic contours span the whole zonal extent of the domain. We demonstrate this minimal requirement for eddy-saturated states using numerical integrations of a single-layer quasi-geostrophic flow over two different topographies characterized by either open or closed geostrophic contours using parameter values loosely inspired by the Southern Ocean. By extending the stability method of Hart [*J. Atmos. Sci.*, **36**, 1736–1746, (1979)] we explain the flow transitions that occur in the solutions with open geostrophic contours and provide insight for the role of the barotropic-topographic instability in producing eddy-saturated states.

1. Introduction

The Southern Ocean, and in particular the Antarctic Circumpolar Current (ACC), are key elements of the climate system. The ACC is driven by a combination of strong westerly winds and buoyancy forcing. Straub (1993) advanced the remarkable hypothesis that the equilibrated ACC zonal transport should be insensitive to the strength of the wind stress forcing. This insensitivity was later verified in eddy-resolving ocean models of the Southern Ocean and is now referred to as *eddy saturation* (Hallberg and Gnanadesikan 2001; Tansley and Marshall 2001; Hallberg and Gnanadesikan 2006; Hogg et al. 2008; Farneti et al. 2010; Meredith et al. 2012; Morisson and Hogg 2013; Munday et al. 2013; Abernathey and Cessi 2014; Farneti et al. 2015; Marshall et al. 2017). A second defining “symptom” of eddy saturation is that, even though the total ACC transport varies very little with wind stress, the domain-averaged eddy kinetic energy (EKE) is approximately linearly related to the wind stress. Finally, a third symptom of eddy saturation is that the total transport increases with bottom drag (Hogg and Blundell 2006; Nadeau and Straub 2012; Nadeau and Ferrari 2015; Marshall et al. 2017).

Some indications of eddy saturation are seen in observations (Böning et al. 2008; Firing et al. 2011). Moreover,

there is evidence that the strength of the westerly winds over the Southern Ocean, which force the ACC, are increasing (Thompson and Solomon 2002; Marshall 2003; Yang et al. 2007; Swart and Fyfe 2012). Recently, Hogg et al. (2015) using satellite altimetry data (*i*) identified a linear trend of the Southern Ocean surface EKE and also (*ii*) found that the ACC zonal transport remains insensitive or even has decreased. This way, Hogg et al. (2015) concluded that the ACC is in an eddy-saturated state. Understanding the mechanisms behind eddy saturation is particularly relevant given the strengthening of the Southern Ocean winds over the last decades, and the potential enhanced strengthening under global warming forcing (Bracegirdle et al. 2013). The question that naturally arises is how will the ACC transport respond to increasing winds?

All previous investigations of eddy saturation, starting with Straub (1993), and continuing with the detailed models of Nadeau and Straub (2009, 2012); Nadeau et al. (2013) and Nadeau and Ferrari (2015), have emphasized the role of baroclinic processes in eddy saturation. Recently, Marshall et al. (2017) and Mak et al. (2017) showed that eddy saturation can emerge as a result of an eddy flux parametrization that was introduced by Marshall et al. (2012). In agreement with Straub (1993), Marshall et al. (2017) relate the production of EKE to the vertical shear of the zonal mean flow. Baroclinic instability is identified as the main source of EKE in all of these explanations of eddy saturation.

*Corresponding author address: Navid C. Constantinou, Scripps Institution of Oceanography, University of California San Diego, La Jolla, CA 92093-0213, USA.

E-mail: navid@ucsd.edu

According to Johnson and Bryden (1989) different density layers are coupled via interfacial form stress that transfers momentum downwards from the sea-surface to the bottom. But at the bottom it is topographic form stress that transfers momentum from the ocean to the solid earth (Munk and Palmén 1951). Note, that in only the standing eddies result in time-mean topographic form stress. Thus, it seems reasonable that topography should play a dominant role in understanding what sets up the total vertically-integrated transport.¹ Arguments about the growth rate of transient baroclinic eddies based on the slope of buoyancy surfaces seem irrelevant to the strength of the standing eddies, and to the pressure–slope correlation that produces the topographic form stress to balance the wind stress. Abernathay and Cessi (2014) showed that isolated topographic features result in localized absolute baroclinic instability located over the topography and an associated almost-barotropic standing wave pattern. Transient eddies are suppressed away from the topography and, relative to the flat-bottom case, the thermocline is shallower and isopycnal slopes are small. Thus, arguments assuming that the isopycnal slopes are so steep as to be marginal with respect to the flat-bottomed baroclinic instability cannot explain eddy saturation in this model configuration with localized topography. In this paper we emphasize the role of the standing eddies, and their form stress, in determining transport in an eddy saturated regime within a barotropic setting.

Indeed, lately there has been increasing evidence arguing for the importance of the barotropic mechanisms in determining the ACC transport. Ward and Hogg (2011) used a 5-layer primitive equation wind-driven model with an ACC-type configuration starting from rest. Following turn-on of the wind a strong barotropic current forms within several days that is able to transfer most of the imparted momentum to the bottom; only after several years does the momentum start being transferred vertically via interfacial form stress. The fast response is that a bottom pressure signal arises a few days after turn-on, and the associated topographic form stress couples the ocean to the solid earth. Subsequently, for about ten years, and contrary to the statistical equilibrium scenario described by Johnson and Bryden (1989), interfacial form stress transfers momentum vertically from the bottom *upwards*. In addition, Thompson and Naveira Garabato (2014), and more recently Youngs et al. (2017), also emphasized the role of the barotropic component of the flow and that of the standing eddies (or standing meanders) in setting up the momentum balance and ACC transport. Furthermore, studies using in situ velocity measurements, satellite altimetry, and output from the Southern Ocean State Estimate (SOSE) also argue in favor of the importance of the barotropic component of the

ACC (Rintoul et al. 2014; Peña Molino et al. 2014; Masich et al. 2015; Donohue et al. 2016).² For example, using measurement from the cDrake experiment Donohue et al. (2016) estimated that the barotropic component of the ACC transport is about 25% of the total transport.

Constantinou and Young (2017) discussed the role of standing eddies using the simplest barotropic model forced by an imposed steady wind stress and retarded by a combination of bottom drag and topographic form stress (Hart 1979; Davey 1980; Holloway 1987; Carnevale and Frederiksen 1987). Constantinou and Young (2017) used a random monoscale topography and argued that a critical requirement for eddy saturation is that the ratio of the planetary potential vorticity (PV) over the topographic PV is large enough so that the geostrophic contours (that is the contours of the planetary plus the topographic contribution to potential vorticity) are “open” in the zonal direction. The main goals of the present paper are:

- (i) to demonstrate that what matters for eddy saturation is the structure of the geostrophic contours and not the actual value of the ratio of the planetary potential vorticity (PV) over the topographic PV,
- (ii) to investigate further whether the barotropic eddy saturation in this model all “symptoms” of eddy saturation observed in eddy resolving ocean models, and
- (iii) to provide insight on how eddy saturation is established in this barotropic setting by studying the instability that gives rise to transient eddies.

We do not claim here that baroclinic processes are not important for setting up the momentum balance in the Southern Ocean. But instead, we emphasize the role of barotropic dynamics and the fact that we can still observe eddy saturation without baroclinicity. We show that this barotropic model with simple deterministic topography and without baroclinic instability, can exhibit impressive eddy saturation with all defining symptoms, provided that the geostrophic contours are open. The model shows (i) insensitivity of the zonal transport to the increase of wind stress forcing, (ii) EKE varying linearly with wind stress and (iii) transport increases with increasing bottom drag (see section 3). In this model, transient eddies arise as an instability due to the interaction of the large-scale zonal flow with the topography. By studying the characteristics of this barotropic–topographic instability we provide insight on the physical mechanism producing eddy saturation in this barotropic model (see section 4).

¹However, some studies provide an explanation to eddy saturation without any, at least direct, reference to the bottom topography (Marshall et al. 2017).

²Usually, the distinction between barotropic and baroclinic components transport imply, respectively, the transport due to the bottom velocity and the “thermal-wind” transport that assumes zero flow at the bottom.

2. Setup

Consider the quasi-geostrophic dynamics of a barotropic fluid of depth $H - h(x, y)$ on a beta-plane. The fluid velocity consisting of a large-scale domain-averaged zonal flow, $U(t)$, along the zonal x direction plus smaller-scale eddies with velocity (u, v) . The eddy component of the flow is derived via an eddy streamfunction $\psi(x, y, t)$ through $(u, v) = (-\partial_y \psi, \partial_x \psi)$; the streamfunction of the total flow is $-U(t)y + \psi(x, y, t)$. The relative vorticity of the flow is $\nabla^2 \psi$, where $\nabla^2 \stackrel{\text{def}}{=} \partial_x^2 + \partial_y^2$, and the quasi-geostrophic potential vorticity (QGPV) of the flow is

$$f_0 + \beta y + \eta + \nabla^2 \psi. \quad (1)$$

In (1), f_0 is the Coriolis parameter at the center of the domain, β is the meridional planetary vorticity gradient and $\eta(x, y) \stackrel{\text{def}}{=} f_0 h(x, y)/H$ is the topographic contribution to QGPV or simply the *topographic PV*. The QGPV and the large-scale flow evolve through:

$$\partial_t \nabla^2 \psi + J(\psi - Uy, \nabla^2 \psi + \eta + \beta y) = -D \nabla^2 \psi, \quad (2a)$$

$$\partial_t U = F - \mu U - \langle \psi \partial_x \eta \rangle, \quad (2b)$$

(Hart 1979; Davey 1980; Holloway 1987; Carnevale and Frederiksen 1987). In (2a) J is the Jacobian, $J(a, b) \stackrel{\text{def}}{=} (\partial_x a)(\partial_y b) - (\partial_y a)(\partial_x b)$, and $D \stackrel{\text{def}}{=} \mu + v_4 \nabla^4$ is the dissipation operator which includes linear Ekman drag μ and hyperviscosity v_4 used for numerical stability. On the right of (2b), $\langle \psi \partial_x \eta \rangle$ is the topographic form stress, with angle brackets denoting an average over the (x, y) -domain. The large-scale flow $U(t)$ in (2b) is forced by the constant $F = \tau / (\rho_0 H)$, where τ is the uniform surface wind stress and ρ_0 is the reference density of the fluid, while is being retarded by a combination of bottom drag and topographic form stress. The domain is periodic in both the zonal and the meridional directions, with size $2\pi L \times 2\pi L$. Following Bretherton and Karweit (1975), we have in mind a mid-ocean region that is smaller than ocean basins but much larger than the length scale of ocean macroturbulence. The role of hyperviscosity is limited only to the removal of small-scale vorticity. Thus the hyperviscosity has a very small effect on larger scales and energy dissipation is mainly due to drag μ .

The model formulated in (2) is the simplest model that can be used to investigate beta-plane turbulence above topography driven by a large-scale zonal wind stress applied at the surface of the fluid. It has been used in the past for studying the interaction of zonal flows with topography (Hart 1979; Davey 1980; Holloway 1987; Carnevale and Frederiksen 1987) and recently by Constantinou and Young (2017) for studying the geostrophic flow regimes above random monoscale topography.

Inspired by the Southern Ocean we take $L = 775$ km, $H = 4$ km, $\rho_0 = 1035$ kg m⁻³, $f_0 = -1.26 \times 10^{-4}$ s⁻¹ and

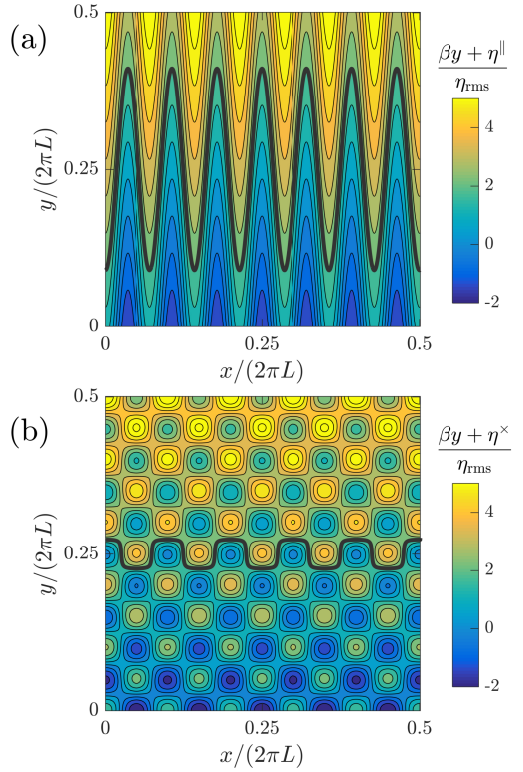


FIG. 1. The structure of the geostrophic contours, $\beta y + \eta$, for the two types of topographies used in this paper: panel (a) uses η^{\parallel} and panel (b) uses η^{\times} . For both cases $\beta \ell_{\eta} / \eta_{\text{rms}} = 0.1$. An open geostrophic contour for each case is marked with a thick curve. The case $\beta y + \eta^{\parallel}$ consists of only open geostrophic contours while $\beta y + \eta^{\times}$ consists of mostly closed ones. (Only a quarter of the flow domain is shown.)

$\beta = 1.14 \times 10^{-11}$ m⁻¹s⁻¹. Also, we take $h_{\text{rms}} \stackrel{\text{def}}{=} \sqrt{\langle h^2 \rangle} = 200$ m, which implies that $\eta_{\text{rms}} = 6.3 \times 10^{-6}$ s⁻¹. For Ekman drag we use $\mu = 6.3 \times 10^{-8}$ s⁻¹ $\approx (180 \text{ day})^{-1}$ (Arbic and Flierl 2004).

Results are reported using two sinusoidal topographies:

$$\eta^{\parallel} = \sqrt{2} \eta_{\text{rms}} \cos(14x/L), \quad (3a)$$

$$\eta^{\times} = 2\eta_{\text{rms}} \cos(10x/L) \cos(10y/L). \quad (3b)$$

Both topographies (3) are monoscale, that is they are characterized by a single length-scale $\ell_{\eta} = \sqrt{\langle \eta^2 \rangle / \langle |\nabla \eta|^2 \rangle}$, which is:

$$\ell_{\eta}^{\parallel} \approx \ell_{\eta}^{\times} = 0.071L = 55.03 \text{ km}.$$

An important factor controlling the behavior of the flow turns out to be the geostrophic contours, that is the level sets of $\beta y + \eta(x, y)$. Figure 1 shows the structure of geostrophic contours for the two topographies η^{\parallel} and η^{\times} using the parameters given above. Here, we distinguish between “open” and “closed” geostrophic contours: open geostrophic contours span the full zonal extent of the domain; see, for

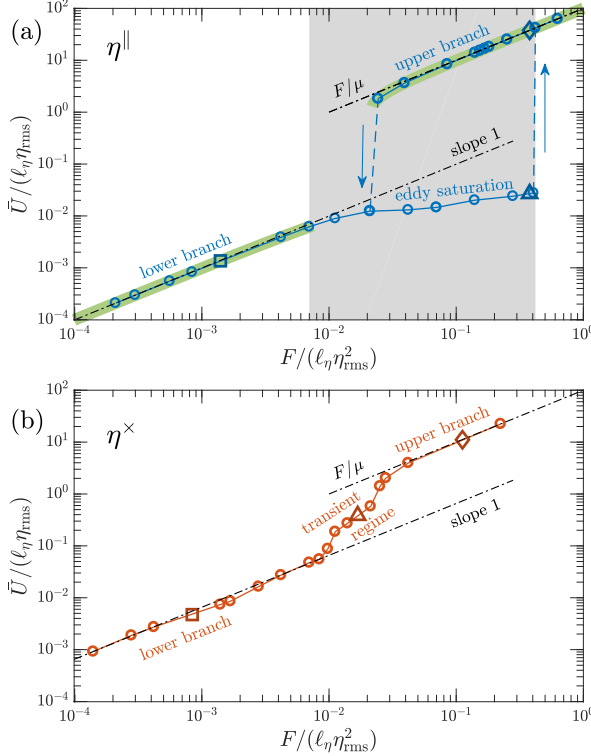


FIG. 2. The equilibrated time-mean large-scale flow \bar{U} as a function of the non-dimensional forcing for the two topographies. Panel (a) shows the case with open geostrophic contours while panel (b) shows the case with closed geostrophic contours. Dash-dotted lines mark the slope 1 and the time-mean large-scale flow $\bar{U} = F/\mu$. In panel (a) the eddy saturation regime $7.0 \times 10^{-3} \leq F/(\ell_\eta \eta_{\text{rms}}^2) \leq 4.1 \times 10^{-1}$ is shaded. The thick semitransparent green curve marks the stability region of the steady solution (9). The points marked with a square \square , a triangle \triangle and a diamond \diamond correspond to the three typical cases for which the energy spectra and flow field snapshots are shown in figures 4 and 5.

example, the two contours marked with thick black curves in each panel of figure 1. For any nonzero β , all geostrophic contours for topography η^\parallel are open while for topography η^\times there exist both closed as well as open geostrophic contours. However, for topography η^\times open geostrophic contours, such as the one shown in figure 1(b), are only found in the vicinity of narrow channels that span the horizontal extent of the domain snaking around local maxima and minima of $\beta y + \eta^\times$. We say, therefore, that η^\times is characterized by closed geostrophic contours.

It is useful to decompose the eddy streamfunction ψ into time-mean “standing eddies” with streamfunction $\bar{\psi}$, and residual “transient eddies” ψ' , so that:

$$\psi(x, y, t) = \bar{\psi}(x, y) + \psi'(x, y, t),$$

where the time-mean is $\bar{\psi} \stackrel{\text{def}}{=} \lim_{T \rightarrow \infty} \frac{1}{T} \int_{t_0}^{t_0+T} \psi(x, y, t') dt'$, with t_0 the time the flow needs to reach a statistically steady

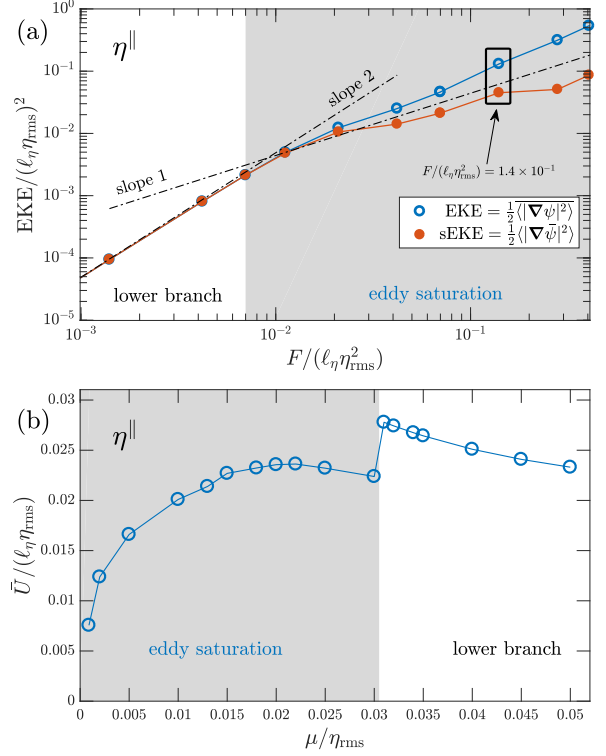


FIG. 3. Panel (a) shows how the equilibrated EKE and the standing wave EKE (sEKE) vary with wind stress forcing for the topography η^\parallel , as the flow transitions from the lower-branch to the eddy saturation regime. Dash-dotted lines mark the slopes 1 and 2. Panel (b) shows how the equilibrated time-mean large-scale flow \bar{U} varies with bottom drag μ in the eddy saturation regime. For these experiments wind stress forcing is kept constant at $F/(\ell_\eta \eta_{\text{rms}}^2) = 1.4 \times 10^{-1}$ (highlighted in panel (a)) while bottom drag μ varies.

state. Similarly, all fields can then be decomposed into time-mean and transient components e.g., $U(t) = \bar{U} + U'(t)$. We are interested in how the time-mean large-scale flow \bar{U} , which is directly related to the time-mean total zonal transport, depends on wind stress forcing F .

3. Results

We report results from numerical solutions of (2) for the two topographies in (3). All solutions presented employ 512^2 grid points; we have verified that results remain unchanged with double the resolution. The hyperviscosity coefficient is set to $v_4 = 2.27 \times 10^9 \text{ m}^4 \text{ s}^{-1}$. The system is evolved using the Exponential Time Differencing 4th-order Runge-Kutta time-stepping scheme (Cox and Matthews 2002; Kassam and Trefethen 2005).³ Time-averaged quantities are calculated by averaging the fields over the interval $30 \leq \mu t \leq 60$.

³The MATLAB code used for solving (2) is available at the github repository: https://github.com/navidcy/QG_ACC_1layer.

a. Variation of the time-mean large-scale flow with wind stress forcing

Figure 2 shows how the time-mean large-scale flow \bar{U} varies with wind stress forcing F for the two topographies. A generic feature of model (2) that characterizes both topographies used here (as well as other more complex and/or multiscale topographies) is the following: as wind stress strength varies from weak to stronger values the flow transitions from a regime with relatively small time-mean large-scale flow \bar{U} to a regime with large \bar{U} . Specifically, for high wind stress forcing values the time-mean large-scale flow becomes $\bar{U} \approx F/\mu$, which is the value for \bar{U} in the flat-bottom case (cf. (2b) with $\eta = 0$). The flat-bottom transport value is marked with the dashed-dotted line in both panels of figure 2. These two flow regimes are referred to as the lower-branch and the upper-branch (Davey 1980), and they are indicated in figure 2. In both branches, the flow reaches a steady state without any transients, after an initial adjustment on the time scale of $O(\mu^{-1})$. For intermediate wind stress forcing values the flow develops transients and becomes turbulent.

In the rest of this subsection we describe in detail the qualitative features of the flow on the lower and upper branches, as well as the transition from one branch to the other for the two topographies.

For weak wind stress forcing F values (i.e. on the lower branch) the equilibrated solutions of (2) are time-independent without any transient eddies. These steady states have a large-scale flow U and an associated stationary eddy flow field ψ that both vary linearly with wind stress forcing F . As a result, EKE varies quadratically with wind stress, i.e., as F^2 . Figure 3(a) shows the variation of EKE with wind stress forcing for topography η^\parallel and confirms the F^2 dependence on the lower branch (similar behavior is found for topography η^\times ; not shown). As the wind stress increases beyond a certain value the lower-branch steady states undergo an instability and begin to develop transients. Even though the topography used here imposes a length-scale ℓ_η , the transient eddies can have scales much smaller than ℓ_η . The onset of this instability is roughly at $F/(\ell_\eta \eta_{\text{rms}}^2) \approx 7 \times 10^{-3}$ for both topographies. (The stability of the lower-branch states for topography η^\parallel is studied in detail in section 4.)

For wind stress forcing values beyond the threshold of the lower-branch instability the flow above the two topographies are qualitatively very different: topography η^\parallel shows eddy saturation while topography η^\times does not.

For topography η^\parallel , as wind stress continues to increase beyond the onset of the transient eddy instability, the time-mean large-scale flow \bar{U} ceases to grow linearly with F ; instead \bar{U} grows at a much slower rate. In fact, \bar{U} shows only a very weak dependence on wind stress strength in the shaded region of figure 2(a): \bar{U} increases only about

4-fold in the course of a 60-fold wind stress increase from $F/(\ell_\eta \eta_{\text{rms}}^2) = 7.0 \times 10^{-3}$ up to 4.1×10^{-1} . This regime is identified as the *eddy saturation regime*. Figure 3(a) shows that in the eddy saturation regime the EKE varies with wind stress forcing at a rate much slower than quadratic. It is also apparent from figure 3(a) that strong transient eddies characterize the eddy saturation regime; this can be seen by the diminishing of the standing wave EKE (sEKE), that is the EKE that results from the standing waves alone.

The barotropic model (2) predicts that for a fully eddy-saturated state, i.e. when \bar{U} does not vary at all with F , the EKE should vary linearly with wind stress forcing. This comes merely as a consequence of the energy power integral, i.e. $\langle -\psi \times (2a) \rangle$ gives:

$$\bar{U} \langle \bar{\psi} \partial_x \eta \rangle + \underbrace{\overline{U' \langle \psi' \partial_x \eta \rangle}}_{\text{negligible}} = 2\mu \underbrace{\langle \frac{1}{2} |\nabla \psi|^2 \rangle}_{\stackrel{\text{def}}{=} \text{EKE}} + \underset{\text{small hyperviscous dissipation}}{\text{.}}$$
(4)

If \bar{U} does not vary with F , then (2b) implies that the form stress $\langle \bar{\psi} \partial_x \eta \rangle$ varies linearly with F and then from (4) we deduce that EKE should also varies linearly with F .

Results from both quasi-geostrophic models (Hogg and Blundell 2006; Nadeau and Straub 2012; Nadeau and Ferrari 2015) and also primitive-equation models (Marshall et al. 2017) demonstrated the somehow counterintuitive fact that in the eddy saturation regime the total transport increases with bottom drag. Here, we show that the barotropic model (2) shows similar behavior in the eddy saturation regime. Figure 3(b) shows how the time-mean large-scale flow \bar{U} varies when wind stress forcing is kept fixed at $F/(\ell_\eta \eta_{\text{rms}}^2) = 1.4 \times 10^{-1}$ while bottom drag μ varies: we find that \bar{U} increases with μ . Within model (2) this is easily rationalized: large bottom drag damps the eddy field ψ , thereby decreasing the form stress. Hence, increased bottom drag strengthens the time-mean large-scale flow \bar{U} , which is necessary to balance the wind stress forcing F in the eddy saturation regime (cf. (2b)). If we increase bottom drag μ beyond a certain threshold the flow laminarizes and transitions from the eddy saturation regime to the lower-branch solution (for the case in figure 3(b) this transition occurs at $\mu/\eta_{\text{rms}} = 3 \times 10^{-2}$). On the lower-branch the time-mean large-scale flow \bar{U} decreases with increasing μ .

The eddy saturation regime in figure 2(a) terminates at $F/(\ell_\eta \eta_{\text{rms}}^2) \approx 4.1 \times 10^{-1}$ by a discontinuous transition to the upper-branch, marked with a dashed vertical line. The upper branch steady solutions are characterized by much larger values of time-mean large-scale flow \bar{U} compared to ones in the eddy saturation regime or on the lower-branch. This discontinuous transition has been coined *drag crisis* (Constantinou and Young 2017). The location of the drag crisis exhibits hysteresis (Charney and DeVore 1979). As we increase wind stress forcing the drag crisis and the transition to the upper branch occurs at $F/(\ell_\eta \eta_{\text{rms}}^2) \approx 4.1 \times 10^{-1}$. However, if we initiate our

model with the upper-branch solutions and start decreasing the wind stress forcing, we can find solutions on the upper branch down to $F/(\ell_\eta \eta_{\text{rms}}^2) \approx 2.44 \times 10^{-2}$: see figure 2(a). We note that one has to be very delicate in initiating the system appropriately to obtain these upper branch solutions. Thus, although the upper-branch solutions shown in figure 2(a) are linearly stable, their basin of attraction is smaller than those of the co-existing eddy-saturated solutions. The extent of the region of multiple stable equilibria is explained by studying the stability of the upper-branch solution (see section 4).

On the other hand, the case with topography with closed geostrophic contours η^\times in figure 2(b), does not exhibit any drag crisis nor any multiple equilibria. More importantly though, topography η^\times does not show any sign of eddy saturation; there is only a slight, barely noticeable, decrease from the linear growth of the time-mean large-scale flow \bar{U} in the $8.0 \times 10^{-4} \leq F/(\ell_\eta \eta_{\text{rms}}^2) \leq 3.0 \times 10^{-3}$, and for those wind stress values the flow does not have any transient eddies. Transient eddies appear for wind stress forcing $F/(\ell_\eta \eta_{\text{rms}}^2) > 4.2 \times 10^{-3}$. For wind stress forcing values beyond the onset of transient eddies the flow transitions from the lower to the upper branch in a continuous manner between $F/(\ell_\eta \eta_{\text{rms}}^2) \approx 8.0 \times 10^{-3}$ and 4.2×10^{-2} .

b. The flow regimes

As described in the previous subsection, we distinguish three qualitatively different flow regimes for each topography. There exist, for both topographies, a lower-branch flow regime for weak wind stress forcing and an upper-branch flow regime for strong wind stress forcing. These flow regimes consist of steady flows without any transient eddies. In between the lower- and upper-branch flow regimes there exists a regime in which the flow has a transient component: the “eddy saturation regime” for topography η^\parallel case and the “transient regime” for topography η^\times . These intermediate regimes are characterized by flows that feature strong transients and are turbulent, especially the eddy saturated case. Moreover, in these regimes the flow shows energy content in a wide range of spatial scales.

The eddy field ψ in the eddy saturated regime is characterized as two-dimensional turbulence. The wind stress F drives directly the large-scale flow U in (2b) and, in turn, U drives the eddy field through the term $U \partial_x \eta$ in (2a). This is a direct transfer of energy from the largest possible scale to the eddies on the length scale of the topography ℓ_η . This turbulent regime is anisotropic; for example, for the case marked with a triangle in figure 2(a) and shown in figure 4(c) the transient eddy velocities are related by $\langle u'^2 \rangle \approx 0.57 \langle v'^2 \rangle$. The eddy flow exhibits energy and enstrophy inertial ranges. The enstrophy inertial range shows a spectral slope close to -3 , as predicted by homogeneous isotropic turbulence arguments. The energy inertial range

produces an inverse transfer of energy from scales ℓ_η to larger scales but, however, it does not show a $-5/3$ spectral slope; on the contrary the energy inertial range shows a positive spectral slope.

Figures 4 and 5 show the energy spectra and a snapshot of the flow fields for a typical representative case of each of the three flow regimes (the cases presented in figures 4 and 5 are the ones marked with a square, a triangle and a diamond in panels (a) and (b) of figure 2). Characteristically, for the open geostrophic contours case (figure 4) the eddy saturated solution shows an energy content in spatial scales other than ℓ_η that is at least eight orders of magnitude larger compared to the steady lower- and upper-branch solutions. Similar behavior is seen for the closed geostrophic contours case of figure 5. The difference between these two cases is that for topography η^\times the lower- and upper- branch solutions are not monochromatic, i.e., they do not have power only at scale ℓ_η : the nonlinearity due to non-vanishing Jacobian term $J(\psi, \eta^\times)$ induces energy to cascade to scales smaller than scale ℓ_η , which is directly forced by the topography.

To elucidate how the zonal momentum balance is shaped by the transient eddies for the two different topographies, we compute the divergence of the eddy PV fluxes, $\nabla \cdot \mathbf{E}$, where

$$\mathbf{E} \stackrel{\text{def}}{=} \left(\overline{(U' + u') \zeta'}, \overline{v' \zeta'} \right). \quad (5)$$

Figure 6 compares the structure of the eddy PV flux divergence (shading) with the time-mean streamlines $\bar{\psi} - \bar{U}y$ (contours) for the two examples shown in figures 4(c) and 5(c). There is an apparent qualitative difference between the two topographies. For the open geostrophic contours case in panel (a) the eddy PV fluxes are dominant over the whole domain and, to a large extent, aligned with the time-mean streamlines. This is not at all the case for the topography with closed geostrophic contours in panel (b). For the model (2), we can verify, by considering the energy budgets among components (Constantinou and Young 2017), that the only transient eddy energy source is the energy conversion from the standing-wave component $\bar{\psi}$ through the term $\langle \bar{\psi} \nabla \cdot \mathbf{E} \rangle$. Thus, the stronger the transient eddies are the more stronger the correlation between eddy PV flux divergence and time-mean streamlines should be. In section 4 we will see that for the case shown in figure 6(a) there is a strong transient-eddy instability that explains this almost-perfect alignment between eddy PV fluxes and time mean streamlines.

Also notice, how the eddy PV fluxes are offset from the topography contours by a quarter wavelength (compare figure 6(a) with figure 1(a)). This offset leads to excitation of a time-mean streamfunction component proportional to $\sin(14x/L)$ that results in large time-mean form stress. To quantify how much the transient eddies shape the mean flow to produce a mean flow component proportional to

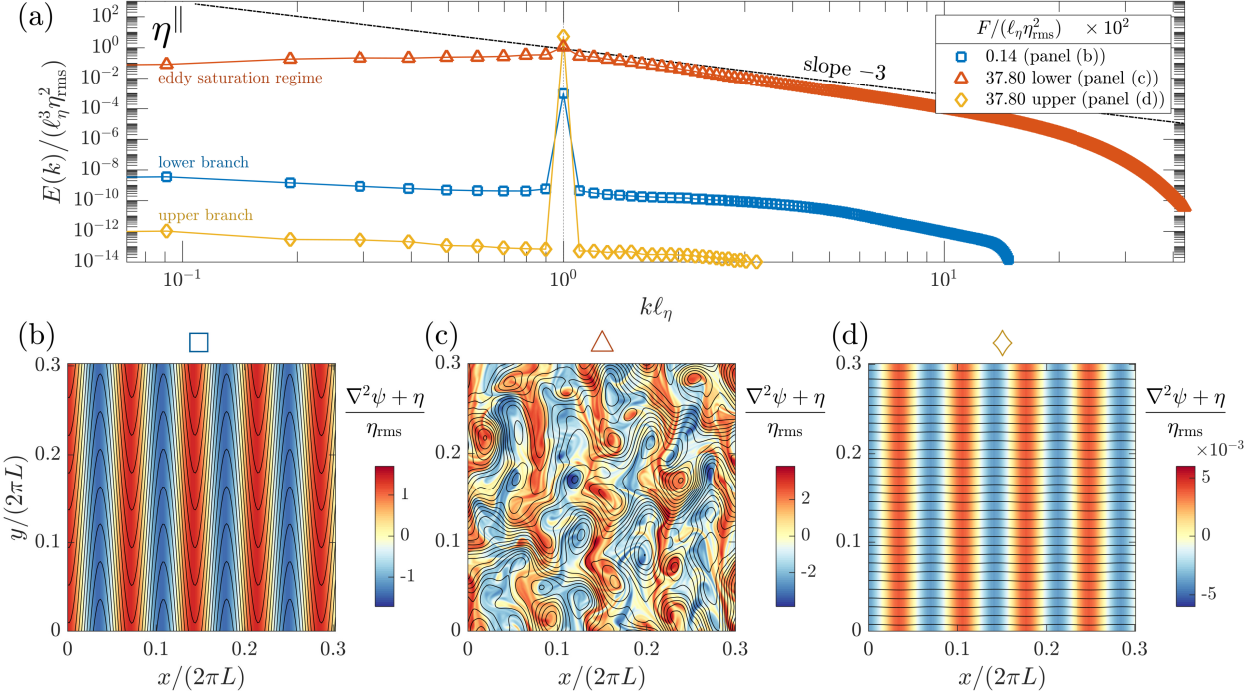


FIG. 4. Panel (a) shows the energy spectra for three typical cases using topography η^\parallel with open geostrophic contours. The dash-dotted line marks the slope -3 prediction for the enstrophy inertial range. Panels (b) to (d) show a final snapshot of the sum of the relative vorticity and the topographic PV, $\nabla^2 \psi + \eta$ (colors) overlayed with the total streamfunction, $\psi - Uy$ (contours), for each of the three cases presented in panel (a). (In panels (b)-(d) only a fraction of the flow domain is shown for better visualization.)

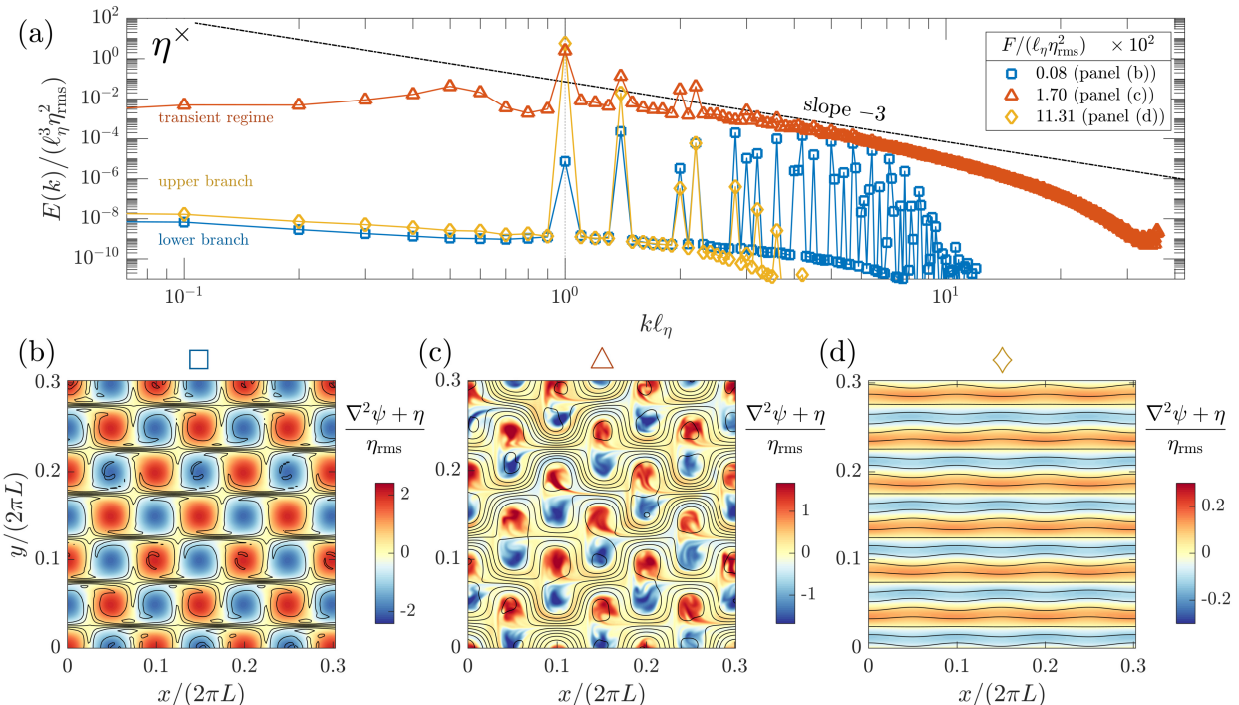


FIG. 5. Same as figure 4 but for three typical cases using topography η^\times with closed geostrophic contours.

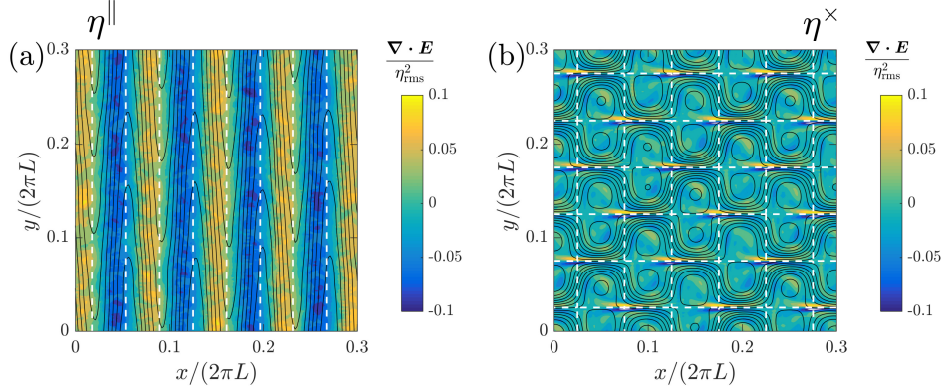


FIG. 6. A comparison of the eddy flux divergence $\nabla \cdot \mathbf{E}$ (colors) with the time-mean streamlines $\bar{\psi} - \bar{U}y$ (black contours) for the two examples marked with a triangle \triangle in figure 2 and also shown in figures 4(c) and 5(c). Dashed white lines mark the $\eta = 0$ contour. For the open geostrophic contours case in panel (a) the eddy PV fluxes are dominant over the whole domain and aligned with the mean flow streamlines. Notice how the eddy PV fluxes are slightly offset from the topography contours thus exciting the $\sin(mx)$ component of the streamfunction.

$\sin(14x/L)$, we compute the correlations:

$$\text{corr}(\cos(14x/L), \nabla \cdot \mathbf{E}) = 0.69, \quad (6a)$$

$$\text{corr}(\sin(14x/L), \nabla \cdot \mathbf{E}) = 0.68, \quad (6b)$$

where $\text{corr}(a, b) \stackrel{\text{def}}{=} \langle ab \rangle / \sqrt{\langle a^2 \rangle \langle b^2 \rangle}$. We find that for the case in figure 6(a) the eddy PV flux divergence projects equally to both $\cos(14x/L)$ and $\sin(14x/L)$ components of the time-mean streamfunction. (For topography η^\times the value of these correlations are at least an order of magnitude less.)

4. The stability of the lower- and upper-branch solutions for topography η^\parallel

For topography of the form $\eta = \eta_0 \cos(mx)$ (as is (3a)) we can understand both the transitions among the three flow regimes as well as the role the transient eddies play on eddy saturation by studying a 3-dimensional invariant manifold of model (2).

It is easy to verify in this case that there is a 3-dimensional invariant manifold by assuming that the eddy streamfunction is:

$$\psi = [S(t) \sin(mx) + C(t) \cos(mx)]/m. \quad (7)$$

Inserting (7) in (2), and because the term $J(\psi, \eta)$ identically vanishes, equations (2) reduce to:

$$\frac{dC}{dt} = -\mu C + m(\beta/m^2 - U)S, \quad (8a)$$

$$\frac{dS}{dt} = -\mu S - m(\beta/m^2 - U)C - \eta_0 U, \quad (8b)$$

$$\frac{dU}{dt} = F - \mu U + \frac{1}{2}\eta_0 S, \quad (8c)$$

(after also ignoring v_4 in D). Steady equilibrium solutions of (8) can be found in the form:

$$U = U^e, \quad \psi(x, y) = \underbrace{[S^e \sin(mx) + C^e \cos(mx)]/m}_{\stackrel{\text{def}}{=} \psi^e}. \quad (9)$$

Both the lower- and upper- branch solutions for the case with topography η^\parallel are *exactly* such steady solutions in the form of (9); see panels (b) and (d) of figure 4. Hart (1979) studied the stability of solutions (9) to perturbations that lie within this invariant manifold. Here, we study the stability of (9) to a general perturbation that may or may not lie within the invariant manifold.

a. Stability calculation

Assume perturbations about the steady state (9):

$$\begin{aligned} U(t) &= U^e + v(t), \\ \psi(x, y, t) &= \psi^e(x, y) + \phi(x, y, t) \\ &\quad + [s(t) \sin(mx) + c(t) \cos(mx)]/m. \end{aligned} \quad (10)$$

In (10) we write the streamfunction perturbation as a sum of a perturbation that lies within the 3-state invariant manifold $[s \sin(mx) + c \cos(mx)]/m$ plus a perturbation ϕ that does not project on the invariant manifold. That said, ϕ satisfies: $\langle \phi e^{imx} \rangle = 0$.

By inserting (10) in (2) and using that (9) is a solution of (8) we get the linearized equations for the perturbations. When projected on the invariant manifold the linearized

equations for the perturbations are:

$$\frac{dc}{dt} = -\mu c + m(\beta/m^2 - U^e)s - mS^e v, \quad (11a)$$

$$\frac{ds}{dt} = -\mu s - m(\beta/m^2 - U^e)c - (\eta_0 - mC^e)v, \quad (11b)$$

$$\frac{dv}{dt} = -\mu v + \frac{1}{2}\eta_0 s, \quad (11c)$$

The orthogonal complement of the linearized equations reads:

$$\partial_t \nabla^2 \phi = -[(U^e \nabla^2 + \beta) \partial_x + \mu \nabla^2] \phi - \left\{ [S^e \cos(mx) - C^e \sin(mx)] (\nabla^2 + m^2) + m\eta_0 \sin(mx) \right\} \partial_y \phi. \quad (12)$$

Eigenanalysis of (11) determines the stability of steady state (9) to perturbations within the invariant manifold; eigenanalysis of (12) determines the stability of (9) to perturbations outside the manifold.

The eigenanalysis of (11) is straightforward and has been studied extensively (Hart 1979; Pedlosky 1981; Källén 1982; Rambaldi and Flierl 1983; Yoden 1985). Charney and Flierl (1980) studied the inviscid and unforced version of (12), i.e., with $\mu = F = 0$ and thus taking the large-scale mean flow U^e as a given parameter. Charney and Flierl (1980) presented expressions for the growth rates in various limits. Here, we perform the stability on the forced-dissipative problem and investigate how this instability may elucidate why eddy saturation is observed.

For the eigenanalysis of (12), first note that if ϕ is independent of y then (12) implies stability. Therefore, a necessary condition instability of (12) is $\partial_y \phi \neq 0$. In this case, also note that:

- (i) (12) is homogeneous in y , i.e., if $\phi(x, y, t)$ is a solution so is $\phi(x, y+a, t)$ for any a , and
- (ii) the coefficients of (12) remain unchanged under $x \mapsto x + 2\pi\kappa/m$ for any integer κ , i.e., if $\phi(x, y, t)$ is a solution so is $\phi(x + 2\pi\kappa/m, y, t)$.

Remark (i) implies that the linear operator in (12) commutes with the translation operator in y and therefore they share the same eigenfunctions. Thus, the eigensolution has y -dependence $\propto e^{in_y y}$. Remark (ii) implies that the linear operator in (12) commutes with the appropriate translation operator by $2\pi\kappa/m$ in x , and thus the eigensolution has an x -dependence in the form of a Bloch wavefunction. (For a more detailed discussion on Bloch eigenfunctions the reader is referred to, for example, the textbook by Ziman (1979) or to the Appendix D of Constantinou (2015).) Thus, we search for the eigensolutions of (12) as:

$$\phi(x, y, t) = e^{\lambda t} e^{in_y y} \tilde{\phi}_{n_x}(x), \quad (13)$$

with

$$\tilde{\phi}_{n_x} \stackrel{\text{def}}{=} e^{in_x x} \sum_{M=-\infty}^{+\infty} c_M e^{iMmx}. \quad (14)$$

In (13) it is understood that the eigenvalue λ depends on n_x and n_y . In (14), n_x is the zonal Bloch wavenumber and it is restricted to take values $|n_x| \leq m/2$ (in condensed matter this is referred to as the first Brillouin zone). To understand why n_x is restricted, consider what (14) (or equivalently remark (ii)) implies regarding the zonal spectral power of ϕ . Eigenfunction ϕ cannot have spectral power in any arbitrary zonal wavenumber, but instead it can have power only at zonal wavenumbers:

$$\pm n_x, \pm(n_x \pm m), \pm(n_x \pm 2m), \dots \quad (15)$$

From (15) we can easily verify that Bloch wavenumbers n_x and $\pm(n_x - m)$ are completely equivalent and thus we only need to study the stability for $|n_x| \leq m/2$ (cf. Ziman (1979); Constantinou (2015)).

With the ansatz (13) we get that for each meridional wavenumber n_y the stability of (12) reduces to the generalized eigenvalue problem:

$$\lambda \nabla_{n_y}^2 \tilde{\phi}_{n_x} = L_{n_y} \tilde{\phi}_{n_x}, \quad (16)$$

where $\nabla_{n_y}^2 \stackrel{\text{def}}{=} \partial_x^2 - n_y^2$ and

$$L_{n_y} \stackrel{\text{def}}{=} -[(U^e \nabla_{n_y}^2 + \beta) \partial_x + \mu \nabla_{n_y}^2] - i n_y \left\{ [S^e \cos(mx) - C^e \sin(mx)] (\nabla_{n_y}^2 + m^2) + m\eta_0 \sin(mx) \right\}. \quad (17)$$

The problem is further reduced if we insert (14) in (16). Then, the eigenproblem (16) reduces into an infinite system of equations whose unknowns are the coefficients c_M and the eigenvalue λ . Truncating the sum in (14) up to $|M| \leq M_{\max}$ leaves us with $2M_{\max} + 1$ equations for $2M_{\max} + 2$ unknowns: $c_{-M_{\max}}, c_{-M_{\max}+1}, \dots, c_{M_{\max}}$ and λ . These equations are compactly written as:

$$A(\lambda) \begin{bmatrix} c_{-M_{\max}} \\ \vdots \\ c_{M_{\max}} \end{bmatrix} = 0, \quad (18)$$

where A is a $(2M_{\max} + 1) \times (2M_{\max} + 1)$ matrix. A non-trivial solution of (18) exists only when $\det[A(\lambda)] = 0$, and this last condition determines the eigenvalues λ that correspond to the eigenfunction with wavenumbers n_x and n_y (Lorenz 1972; Gill 1974; Charney and Flierl 1980).

b. Stability results

We perform the stability of the steady state (9) for the topography η^{\parallel} with respect to both (11) and (12). The region of stability of the steady state (9) with respect to both (11) and (12) is marked with the thick semitransparent curve in figure 2(a), both for the lower- and for the upper-flow regime. The appearance of transient eddies as wind stress is increased, as well as the termination of the upper-branch

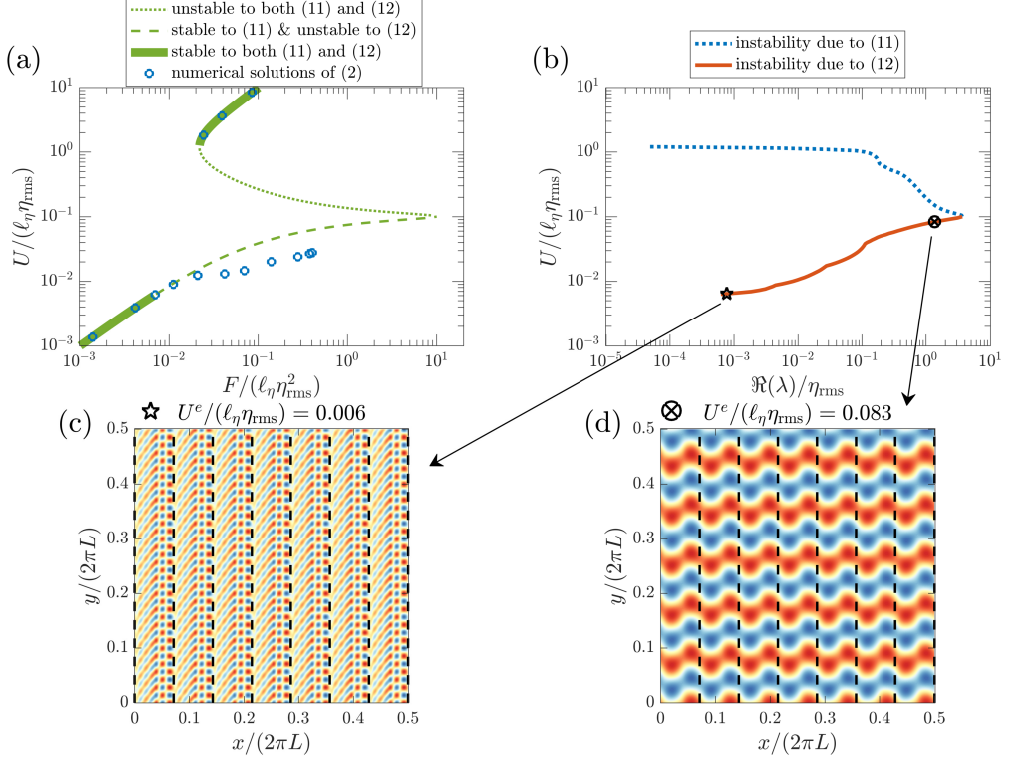


FIG. 7. Panel (a) shows the steady solutions (9) for topography η^{\parallel} and their stability as predicted by (11) and (12). Also shown for comparison are the numerical solutions of (2) with circles. Panel (b) shows the instability growth rates, i.e., the real part of the eigenvalue λ , according to (11) and (12). Only unstable eigenvalues are shown. The structure of the most unstable eigenfunction that correspond to U^e just above the marginal point for instability is shown in panel (c), while the eigenfunction for U^e just before maximum instability is shown in panel (d) (these are the two cases marked in panel (b)). The eigenfunction in panel (c) has $n_y = 2.5m$ and Bloch wavenumber $n_x = m/2$; the eigenfunction in panel (d) has $n_y = m$ and Bloch wavenumber $n_x = 0$. The dashed black lines mark the topographic PV wavelength. Notice that only part of the domain is shown for clarity. (The eigenfunctions were obtained with eigenanalysis of (16).)

solution as wind stress is decreased, are both identified with the onset of an instability of the lower- and upper-branch solutions (9) respectively. Figure 7 shows the large-scale flow U^e of the steady state (9) as a function of wind stress forcing F , together with their stability, as predicted by (11) and (12), and also the numerical results of (2) for comparison. It is clear that the transition from the lower branch to the turbulent regime, in which eddy saturation is observed, is triggered by the instability due to (11) rather than by (11). This instability of the lower branch first occurs at $F/(\ell_\eta \eta_{\text{rms}}^2) = 7.15 \times 10^{-3}$. Figure 7(c) shows the most unstable eigenfunction just beyond the marginal point of instability. This eigenfunction has a small-scale meridional structure; the meridional wavenumber of the eigenfunction shown in figure 7(c) is $n_y = 2.5m$. Thus, the instability of the lower branch due to (11) introduces y -dependence in the flow; see figure 7(c).

Next, we would like to investigate how this instability contributes to the occurrence of eddy saturation. What turns out to be very interesting is how the instability growth rate varies with the large-scale flow U^e . Figure 7(b) shows that,

in the regime which we find eddy saturation, the instability growth rate due to (11) increases dramatically with U^e ; growth rates increase by a factor of 10^3 while U^e increases by only a factor of 15. The transient eddy source, thus, increases significantly for small changes in U . In this way, and by analogy with arguments for baroclinic eddy saturation, larger wind stress forcing implies the need for stronger eddies and this leads to eddy saturation. Furthermore, this argues that the flow adjusts to a state close to marginal stability for this barotropic-topographic instability, similarly to the baroclinic marginal stability argument (Stone 1978).

The stability calculations presented in this section are based on that the topography does not depend on y . However, the same flow transitions occur for flows with open geostrophic contours above complex topographies. In that case, finding the lower- and upper-branch equilibrium steady states is much more painful since some of the Jacobian terms, for example $J(\psi^e, \eta)$, are *not* identically zero. Therefore, the lower- and upper-branch solutions do not lie within any low-dimensional manifold. Methods for obtain-

ing such equilibria were developed by Tung and Rosenthal (1985).

5. Discussion

The results reported here demonstrate that eddy saturation can occur even without baroclinicity. A bare barotropic setting is capable of producing an eddy saturation regime with all three signature features, that is,

- (i) transport being insensitive to wind stress forcing,
- (ii) EKE varying close to linearly with wind stress forcing instead of quadratically, and
- (iii) transport increases with increasing bottom drag.

The factor which controls the appearance or not of eddy saturated states in a barotropic setting is whether or not the geostrophic contours are open. This was demonstrated here this using two simple sinusoidal topographies that bare this distinction.

For the y -independent topography with open geostrophic contours η^{\parallel} , we extended the stability analysis of Hart (1979) to encompass any general flow perturbations. Thus, we managed to identify the various flow transitions shown in figure 2(a) with the onset of an instability. The stability calculations presented section 4 crucially depend on that the topography η^{\parallel} does not depend on y . However, in the context of this barotropic model, we expect that the same flow transitions for flow above more complex topography $\eta(x, y)$ with open geostrophic contours would result from the same barotropic-topographic instability.

At first glance the results reported here might seem to come in contrast with previous results in baroclinic quasi-geostrophic models of the Southern Ocean. For example, Nadeau and Ferrari (2015) using a two-layer quasi-geostrophic model with channel walls at the Northern and Southern boundaries and with a meridional-ridge topography and found that eddy saturation appeared when the geostrophic contours where “closed” or “blocked”. However, this apparent disagreement stems mainly from the fact that the characterization of “open” and “closed” geostrophic contours is not very concrete. Nadeau and Ferrari (2015) show in the bottom-right panel of figure 8 in their paper the structure of the geostrophic contours for a case when they find eddy saturation. They characterized the geostrophic contours as “closed” or “blocked”. However, if they did not have boundaries in the meridional direction then this geostrophic contours would exactly resemble the case shown in figure 3(a) and which here we were referring to as “open”.

We note, that the flow characteristics that were described in section 3 are not quirks of the simple sinusoidal topographies (3). The eddy saturation regime, the drag crisis, and multiple equilibria that are present here when geostrophic contours are open, have been all also recently found to

exist in this model for a flow above a random monoscale topography with open geostrophic contours (Constantinou and Young 2017) and also above a multi-scale topography that has a k^{-2} power spectrum (not reported).

In conclusion, the results presented here emphasized that barotropic processes might play a role in eddy saturation. In particular, they can be partly responsible for eddy saturation, at least for component the transport that is related to the bottom-reference flow velocity of the ACC. (This, so called barotropic transport, is about 25% of the total transport, according to Donohue et al. (2016).) Even though the ACC is strongly affected by baroclinic processes, our results here reinforce the increasing evidence arguing for the importance of the barotropic mechanisms in determining the ACC transport (Ward and Hogg 2011; Thompson and Naveira Garabato 2014; Youngs et al. 2017).

Acknowledgments. I am mostly grateful to William Young for his support and his insightful comments. Discussions with Petros Ioannou, Spencer Jones, Sean Haney, Louis-Philippe Nadeau, Cesar Rocha, Andrew Thompson, Gregory Wagner, and Till Wagner are greatly acknowledged. I also thank David Straub for his constructive review comments. This project was supported by the NOAA Climate and Global Change Postdoctoral Fellowship Program, administered by UCAR’s Cooperative Programs for the Advancement of Earth System Sciences.

References

- Abernathey, R., and P. Cessi, 2014: Topographic enhancement of eddy efficiency in baroclinic equilibration. *J. Phys. Oceanogr.*, **44** (8), 2107–2126, doi:10.1175/JPO-D-14-0014.1.
- Arbic, B. K., and G. R. Flierl, 2004: Baroclinically unstable geostrophic turbulence in the limits of strong and weak bottom Ekman friction: Application to midocean eddies. *J. Phys. Oceanogr.*, **34** (10), 2257–2273, doi:10.1175/1520-0485(2004)034<2257:BUGTIT>2.0.CO;2.
- Böning, C. W., A. Dispert, M. Visbeck, S. R. Rintoul, and F. U. Schwarzkopf, 2008: The response of the Antarctic Circumpolar Current to recent climate change. *Nat. Geosci.*, **1** (1), 864–869, doi:10.1038/ngeo362.
- Bracegirdle, T. J., E. Shuckburgh, J.-B. Sallee, Z. Wang, A. J. S. Meijers, N. Bruneau, T. Phillips, and L. J. Wilcox, 2013: Assessment of surface winds over the Atlantic, Indian, and Pacific Ocean sectors of the Southern Ocean in CMIP5 models: historical bias, forcing response, and state dependence. *J. Geophys. Res.-Atmospheres*, **118** (2), 547–562, doi:10.1002/jgrd.50153.
- Bretherton, F. P., and M. Karweit, 1975: Mid-ocean mesoscale modeling. *Numerical models of ocean circulation*, National Academy of Sciences, 237–249.
- Carnevale, G. F., and J. S. Frederiksen, 1987: Nonlinear stability and statistical mechanics of flow over topography. *J. Fluid Mech.*, **175**, 157–181, doi:10.1017/S002211208700034X.
- Charney, J. G., and J. G. DeVore, 1979: Multiple flow equilibria in the atmosphere and blocking. *J. Atmos. Sci.*, **36**, 1205–1216, doi:10.1175/1520-0469(1979)036<1205:MFEITA>2.0.CO;2.

- Charney, J. G., and G. R. Flierl, 1980: Oceanic analogues of large-scale atmospheric motions. *Evolution of Physical Oceanography*, B. A. Warren, and C. Wunsch, Eds., The MIT Press, chap. 18.
- Constantinou, N. C., 2015: Formation of large-scale structures by turbulence in rotating planets. Ph.D. thesis, National and Kapodistrian University of Athens, Athens, URL <https://arxiv.org/abs/1503.07644>, (arXiv:1503.07644).
- Constantinou, N. C., and W. R. Young, 2017: Beta-plane turbulence above monoscale topography. *J. Fluid Mech.*, **827**, 415–447, doi:10.1017/jfm.2017.482.
- Cox, S. M., and P. C. Matthews, 2002: Exponential time differencing for stiff systems. *J. Comput. Phys.*, **176** (2), 430–455, doi:10.1006/jcph.2002.6995.
- Davey, M. K., 1980: A quasi-linear theory for rotating flow over topography. Part 1. Steady β -plane channel. *J. Fluid Mech.*, **99** (02), 267–292, doi:10.1017/S0022112080000614.
- Donohue, K. A., K. L. Tracey, D. R. Watts, M. P. Chidichimo, and T. K. Chereskin, 2016: Mean Antarctic Circumpolar Current transport measured in Drake Passage. *Geophys. Res. Lett.*, **43**, 11 760–11 767, doi:10.1002/2016GL070319.
- Farneti, R., T. L. Delworth, A. J. Rosati, S. M. Griffies, and F. Zeng, 2010: The role of mesoscale eddies in the rectification of the Southern Ocean response to climate change. *J. Phys. Oceanogr.*, **40**, 1539–1557, doi:10.1175/2010JPO4353.1.
- Farneti, R., and Coauthors, 2015: An assessment of Antarctic Circumpolar Current and Southern Ocean meridional overturning circulation during 1958–2007 in a suite of interannual CORE-II simulations. *Ocean Model.*, **93**, 84–120, doi:10.1016/j.ocemod.2015.07.009.
- Firing, Y. L., T. K. Chereskin, and M. R. Mazloff, 2011: Vertical structure and transport of the Antarctic Circumpolar Current in Drake Passage from direct velocity observations. *J. Geophys. Res.-Oceans*, **116** (C8), C08015, doi:10.1029/2011JC006999.
- Gill, A. E., 1974: The stability of planetary waves on an infinite beta-plane. *Geophys. Astrophys. Fluid Dyn.*, **6**, 29–47, doi:10.1080/03091927409365786.
- Hallberg, R., and A. Gnanadesikan, 2001: An exploration of the role of transient eddies in determining the transport of a zonally reentrant current. *J. Phys. Oceanogr.*, **31** (11), 3312–3330, doi:10.1175/1520-0485(2001)031<3312:AEOTRO>2.0.CO;2.
- Hallberg, R., and A. Gnanadesikan, 2006: The role of eddies in determining the structure and response of the wind-driven Southern Hemisphere overturning: Results from the modeling eddies in the Southern Ocean (MESO) project. *J. Phys. Oceanogr.*, **36**, 2232–2252, doi:10.1175/JPO2980.1.
- Hart, J. E., 1979: Barotropic quasi-geostrophic flow over anisotropic mountains. *J. Atmos. Sci.*, **36** (9), 1736–1746, doi:10.1175/1520-0469(1979)036<1736:BQGFOA>2.0.CO;2.
- Hogg, A. M., and J. R. Blundell, 2006: Interdecadal variability of the Southern Ocean. *J. Phys. Oceanogr.*, **36**, 1626–1645, doi:10.1175/JPO2934.1.
- Hogg, A. M., M. P. Meredith, J. R. Blundell, and C. Wilson, 2008: Eddy heat flux in the Southern Ocean: Response to variable wind forcing. *J. Climate*, **21**, 608–620, doi:10.1175/2007JCLI1925.1.
- Hogg, A. M., M. P. Meredith, D. P. Chambers, E. P. Abrahamsen, C. W. Hughes, and A. K. Morrison, 2015: Recent trends in the Southern Ocean eddy field. *J. Geophys. Res.-Oceans*, **120**, 1–11, doi:10.1002/2014JC010470.
- Holloway, G., 1987: Systematic forcing of large-scale geophysical flows by eddy-topography interaction. *J. Fluid Mech.*, **184**, 463–476, doi:10.1017/S0022112087002970.
- Johnson, G. C., and H. L. Bryden, 1989: On the size of the Antarctic Circumpolar Current. *Deep-Sea Res.*, **36** (1), 39–53, doi:10.1016/0198-0149(89)90017-4.
- Källén, E., 1982: Bifurcation properties of quasigeostrophic, barotropic models and their relation to atmospheric blocking. *Tellus*, **34** (3), 255–265, doi:10.1111/j.2153-3490.1982.tb01814.x.
- Kassam, A.-K., and L. N. Trefethen, 2005: Fourth-order time-stepping for stiff PDEs. *SIAM J. Sci. Comput.*, **26** (4), 1214–1233, doi:10.1137/S1064827502410633.
- Lorenz, E. N., 1972: Barotropic instability of Rossby wave motion. *J. Atmos. Sci.*, **29**, 258–269, doi:10.1175/1520-0469(1972)029<0258:BIORWM>2.0.CO;2.
- Mak, J., D. P. Marshall, J. R. Maddison, and S. D. Bachman, 2017: Emergent eddy saturation from an energy constrained parameterisation. *Ocean Model.*, **112**, 125–138, doi:10.1016/j.ocemod.2017.02.007.
- Marshall, D. P., M. H. P. Abbaum, J. R. Maddison, D. R. Munday, and L. Novak, 2017: Eddy saturation and frictional control of the Antarctic Circumpolar Current. *Geophys. Res. Lett.*, **44**, doi:10.1002/2016GL071702.
- Marshall, D. P., J. R. Maddison, and P. S. Berloff, 2012: A framework for parameterizing eddy potential vorticity fluxes. *J. Phys. Oceanogr.*, **42**, 539–557, doi:10.1175/JPO-D-11-048.1.
- Marshall, G. J., 2003: Trends in the Southern Annular Mode from observations and reanalyses. *J. Climate*, **16**, 4134–4143, doi:10.1175/1520-0442(2003)016<4134:TSAM>2.0.CO;2.
- Masich, J., T. K. Chereskin, and M. R. Mazloff, 2015: Topographic form stress in the Southern Ocean State Estimate. *J. Geophys. Res.-Oceans*, **120** (12), 7919–7933, doi:10.1002/2015JC011143.
- Meredith, M. P., A. C. Naveira Garabato, A. M. Hogg, and R. Farneti, 2012: Sensitivity of the overturning circulation in the Southern Ocean to decadal changes in wind forcing. *J. Climate*, **25**, 99–110, doi:10.1175/2011JCLI4204.1.
- Morisson, A. K., and A. M. Hogg, 2013: On the relationship between Southern Ocean overturning and ACC transport. *J. Phys. Oceanogr.*, **43**, 140–148, doi:10.1175/JPO-D-12-057.1.
- Munday, D. R., H. L. Johnson, and D. P. Marshall, 2013: Eddy saturation of equilibrated circumpolar currents. *J. Phys. Oceanogr.*, **43**, 507–532, doi:10.1175/JPO-D-12-095.1.
- Munk, W. H., and E. Palmén, 1951: Note on the dynamics of the Antarctic Circumpolar Current. *Tellus*, **3**, 53–55, doi:10.1111/j.2153-3490.1951.tb00776.x.
- Nadeau, L.-P., and R. Ferrari, 2015: The role of closed gyres in setting the zonal transport of the Antarctic Circumpolar Current. *J. Phys. Oceanogr.*, **45**, 1491–1509, doi:10.1175/JPO-D-14-0173.1.
- Nadeau, L.-P., and D. N. Straub, 2009: Basin and channel contributions to a model Antarctic Circumpolar Current. *J. Phys. Oceanogr.*, **39** (4), 986–1002, doi:10.1175/2008JPO4023.1.

- Nadeau, L.-P., and D. N. Straub, 2012: Influence of wind stress, wind stress curl, and bottom friction on the transport of a model Antarctic Circumpolar Current. *J. Phys. Oceanogr.*, **42** (1), 207–222, doi:[10.1175/JPO-D-11-058.1](https://doi.org/10.1175/JPO-D-11-058.1).
- Nadeau, L.-P., D. N. Straub, and D. M. Holland, 2013: Comparing idealized and complex topographies in quasigeostrophic simulations of an Antarctic Circumpolar Current. *J. Phys. Oceanogr.*, **43** (8), 1821–1837, doi:[10.1175/JPO-D-12-0142.1](https://doi.org/10.1175/JPO-D-12-0142.1).
- Pedlosky, J., 1981: Resonant topographic waves in barotropic and baroclinic flows. *J. Atmos. Sci.*, **38** (12), 2626–2641, doi:[10.1175/1520-0469\(1981\)038<2626:RTWIBA>2.0.CO;2](https://doi.org/10.1175/1520-0469(1981)038<2626:RTWIBA>2.0.CO;2).
- Peña Molino, B., S. R. Rintoul, and M. R. Mazloff, 2014: Barotropic and baroclinic contributions to along-stream and across-stream transport in the Antarctic Circumpolar Current. *J. Geophys. Res.-Oceans*, **119** (11), 8011–8028, doi:[10.1002/2014JC010020](https://doi.org/10.1002/2014JC010020).
- Rambaldi, S., and G. R. Flierl, 1983: Form drag instability and multiple equilibria in the barotropic case. *Il Nuovo Cimento C*, **6** (5), 505–522, doi:[10.1007/BF02561449](https://doi.org/10.1007/BF02561449).
- Rintoul, S. R., S. Sokolov, M. J. M. Williams, B. Peña Molino, M. Rosenberg, and N. L. Bindoff, 2014: Antarctic Circumpolar Current transport and barotropic transition at Macquarie Ridge. *Geophys. Res. Lett.*, **41** (20), 7254–7261, doi:[10.1002/2014GL061880](https://doi.org/10.1002/2014GL061880).
- Stone, P. H., 1978: Baroclinic adjustment. *J. Atmos. Sci.*, **35**, 561–571, doi:[10.1175/1520-0469\(1978\)035<0561:BA>2.0.CO;2](https://doi.org/10.1175/1520-0469(1978)035<0561:BA>2.0.CO;2).
- Straub, D. N., 1993: On the transport and angular momentum balance of channel models of the Antarctic Circumpolar Current. *J. Phys. Oceanogr.*, **23**, 776–782, doi:[10.1175/1520-0485\(1993\)023<0776:OTTAAM>2.0.CO;2](https://doi.org/10.1175/1520-0485(1993)023<0776:OTTAAM>2.0.CO;2).
- Swart, N. C., and J. C. Fyfe, 2012: Observed and simulated changes in the Southern Hemisphere surface westerly wind-stress. *Geophys. Res. Lett.*, **39** (16), L16 711, doi:[10.1029/2012GL052810](https://doi.org/10.1029/2012GL052810).
- Tansley, C. E., and D. P. Marshall, 2001: On the dynamics of wind-driven circumpolar currents. *J. Phys. Oceanogr.*, **31**, 3258–3273, doi:[10.1175/1520-0485\(2001\)031<3258:OTDOWD>2.0.CO;2](https://doi.org/10.1175/1520-0485(2001)031<3258:OTDOWD>2.0.CO;2).
- Thompson, A. F., and A. C. Naveira Garabato, 2014: Equilibration of the Antarctic Circumpolar Current by standing meanders. *J. Phys. Oceanogr.*, **44** (7), 1811–1828, doi:[10.1175/JPO-D-13-0163.1](https://doi.org/10.1175/JPO-D-13-0163.1).
- Thompson, D. W. J., and S. Solomon, 2002: Interpretation of recent Southern Hemisphere climate change. *Science*, **296**, 895–899, doi:[10.1126/science.1069270](https://doi.org/10.1126/science.1069270).
- Tung, K.-K., and A. J. Rosenthal, 1985: Theories of multiple equilibria – A critical reexamination. Part I: Barotropic models. *J. Atmos. Sci.*, **42**, 2804–2819, doi:[10.1175/1520-0469\(1985\)042<2804:TOMEAC>2.0.CO;2](https://doi.org/10.1175/1520-0469(1985)042<2804:TOMEAC>2.0.CO;2).
- Ward, M. L., and A. M. Hogg, 2011: Establishment of momentum balance by form stress in a wind-driven channel. *Ocean Model.*, **40** (2), 133–146, doi:[10.1016/j.ocemod.2011.08.004](https://doi.org/10.1016/j.ocemod.2011.08.004).
- Yang, X.-Y., R. X. Huang, and D. X. Wang, 2007: Decadal changes of wind stress over the Southern Ocean associated with Antarctic ozone depletion. *J. Climate*, **20** (14), 3395–3410, doi:[10.1175/JCLI4195.1](https://doi.org/10.1175/JCLI4195.1).
- Yoden, S., 1985: Bifurcation properties of a quasi-geostrophic, barotropic, low-order model with topography. *J. Meteor. Soc. Japan. Ser. II*, **63** (4), 535–546.
- Youngs, M. K., A. F. Thompson, A. Lazar, and K. J. Richards, 2017: ACC meanders, energy transfer, and mixed barotropic–baroclinic instability. *J. Phys. Oceanogr.*, **47**, 1291–1305, doi:[10.1175/JPO-D-16-0160.1](https://doi.org/10.1175/JPO-D-16-0160.1).
- Ziman, J. M., 1979: *Principles of the Theory of Solids*. 2nd ed., Cambridge University Press.